Konrad-Zuse-Zentrum
für Informationstechnik Berlin

Takustraße 7
D-14195 Berlin-Dahlem
Germany

J. LANG, B. ERDMANN, M. SEEBASS [1]

Impact of Nonlinear Heat Transfer on Temperature Control in Regional Hyperthermia

[1]The work of this author was supported by Deutsche Forschungsgemeinschaft, Sonderforschungsbereich 273, Germany

Preprint SC 97–73 (December 1997)

Impact of Nonlinear Heat Transfer on Temperature Control in Regional Hyperthermia

Jens Lang, Bodo Erdmann, Martin Seebass

Konrad–Zuse–Zentrum für Informationstechnik Berlin
Takusstr. 7, 14195 Berlin, Germany.
e–mail: {lang,erdmann,seebass}@zib.de

Abstract. We describe an optimization process specially designed for regional hyperthermia of deep seated tumors in order to achieve desired steady–state temperature distributions. A nonlinear three–dimensional heat transfer model based on temperature–dependent blood perfusion is applied to predict the temperature. Using linearly implicit methods in time and adaptive multilevel finite elements in space, we are able to integrate efficiently the instationary nonlinear heat equation with high accuracy. Optimal heating is obtained by minimizing an integral object function which measures the distance between desired and model predicted temperatures. A sequence of minima is calculated from successively improved constant–rate perfusion models employing a damped Newton method in an inner iteration. We compare temperature distributions for two individual patients calculated on coarse and fine spatial grids and present numerical results of optimizations for a Sigma 60 Applicator of the BSD 2000 Hyperthermia System.

Index Terms: Hyperthermia, nonlinear heat transfer, optimization, mesh control, finite elements

1 Introduction

Hyperthermia, i.e., heating tissue to 42 - 43°C, is a method of cancer therapy. It is normally applied as an additive therapy to enhance the effect of conventional radio- or chemotherapy. The standard way to produce local heating in the human body is the use of electromagnetic waves. We are mainly interested in regional hyperthermia of deep seated tumors. For this type of treatment usually a phased array of antennas surrounding the patient is used (see Fig. 2). The distribution of absorbed power within the patient's body can be steered by selecting the amplitudes and phases of the antennas' driving voltages. The space between the body and the antennas is filled by a so-called water bolus to avoid excessive heating of the skin.

From the viewpoint of computational medicine there are different challenges:
(i) modelling and calculation of the electromagnetic field and the forced temperature, (ii) optimization of the channel adjustments to achieve favourable interference patterns for a successful cancer therapy, (iii) visualization of vector fields and temperature distributions on a very complicated geometry. It should be possible to perform all steps of a simulation for each individual patient within a medical planning system [1].

The purpose of our paper is to describe an optimization process based on a three–dimensional nonlinear heat transfer model. Finite element solutions of the electromagnetic fields [2] are taken as input data. It is a rather difficult task to establish an appropriate physical model for the heat transport in the human body. Several approaches can be found in the literature (see eg. [18, 10]). The basis for our modelling is Pennes' bio–heat–transfer equation which we equip with a temperature–dependent blood perfusion. A similar two–dimensional model was studied in [17] for ferromagnetic thermoseed hyperthermia.

The optimization process is based on a specially designed object function. Our aim is to achieve a stationary temperature distribution which avoids "hot spots" (temperature greater than 44°C) in healthy tissue and "cold spots" (temperature less than 42°C) in the tumor region. In order to derive a fast optimization we approximate the nonlinear model by a sequence of linear ones which can be optimized very fast by applying a superposition principle. Besides an optimized stationary temperature distribution we are also interested in getting informations about the time–dependent heating process. These informations can be used for comparison with available clinical data about the transient phases at the beginning and the end of the treatment.

The simulation of the present heat transfer model requires the numerical solution of a time–dependent partial differential equation in a complex geometry involving a nonlinearity due to the perfusion term and different material properties of the

tissues. The temperature is highly nonuniformly distributed in space and time. In such a situation adaptive algorithms which have been an object of continuing investigations during the last years are often the only way to get an accurate solution with an acceptable amount of computational time and memory requirements. Adaptive multilevel finite element methods have been developed by the authors to solve problems with highly nonuniform solutions [4, 3, 11]. In order to achieve a prescribed accuracy the proposed methods are essentially based on repeated application of three steps: solving discretized equations, error estimation, and local refinement. The final spatial grids are well adapted to the solution. Linearly implicit integrators with step size control are used to integrate the equation in time. The implementation of those complex algorithms requires modern software design and programming languages as C or C++. Our code KARDOS is based on the programming environment KASKADE [4]. Additionally, a comfortable visualization tool is invaluable. We use the graphical system HYPERPLAN [1] for the presentation of our numerical results.

The paper is organized as follows: In Section 2 we explain our mathematical modelling of regional hyperthermia based on a nonlinear heat transfer model and establish the object function for the optimization. In Section 3 we present an adaptive numerical algorithm for the solution of the nonlinear heat equation. A posteriori error estimates are derived to control the spatial discretization in each time step. The optimization process is described. Numerical results are presented in Section 4. We end up with some conclusions in Section 5.

2 Mathematical Modelling of Regional Hyperthermia

2.1 Nonlinear Heat Transfer Model

The basic model used in our simulation is the instationary bio–heat–transfer equation proposed by Pennes [14]

$$\rho c \frac{\partial T}{\partial t} = \operatorname{div}(\kappa \operatorname{grad} T) - c_b W (T - T_b) + Q_e \,, \tag{1}$$

where ρ is the density, c and c_b are specific heat of tissue and blood, κ is the thermal conductivity; T_b is the blood temperature; W is the mass flow rate of blood per unit volume of tissue. The power Q_e deposited by an electric field E in a tissue with electric conductivity σ is given by

$$Q_e = \frac{1}{2}\sigma |E|^2 \,. \tag{2}$$

In hyperthermia applicators utilizing electromagnetic waves the antennas normally

are grouped into *channels* that can be independently controlled. For such an applicator the total electric field E can be computed by superposition

$$E = \sum_{j=1}^{N_{chan}} a_j \; exp(-i\theta_j) \; E_j, \tag{3}$$

where the channel j has amplitude a_j and phase delay θ_j. E_j is the electric field generated by the antennas of channel j. If complex values z_j are defined as

$$z_j = a_j \; exp(-i\theta_j) \tag{4}$$

the absorbed power Q_e can be expressed as a quadratic function of z_j

$$Q_e = \frac{1}{2}\sigma \sum_{j,k=1}^{N_{chan}} z_j^* E_j^* E_k z_k \; . \tag{5}$$

Besides the differential equation boundary conditions determine the temperature distribution. The heat exchange between body and water bolus can be described by the flux condition

$$\kappa \frac{\partial T}{\partial n} = \beta (T_{bol} - T) \tag{6}$$

where T_{bol} is the bolus temperature and β is the heat transfer coefficient. No heat loss is assumed in remaining regions. We use for our simulations $\beta = 45 W/m^2/^oC$ and $T_{bol} = 25^oC$.

Studies that predict temperatures in tissue models usually assume a constant–rate blood perfusion within each tissue. However, several experiments have shown that the response of vasculature in tissues to heat stress is strongly temperature–dependent [16]. When heated up to $41-43^oC$, temperatures that are commonly used in clinical hyperthermia, the blood flow in normal tissues, e.g., skin and muscle, increases significantly. In contrast, the tumor zone often appears to be so vulnerable to heat that the blood flow decreases on heating.

For later computations it is useful to split the temperature. The stationary temperature field T can be computed as sum of the basal temperature T_{bas} determined by $Q_e = 0$, and the temperature increment T_{inc} caused by the hyperthermic application. We easily derive the stationary equations for T_{bas} and T_{inc}

$$\begin{aligned} \operatorname{div}(\kappa \operatorname{grad} T_{bas}) - c_b W[T_{bas}](T_{bas} - T_b) &= 0\,, \\ \kappa \frac{\partial T_{bas}}{\partial n} - \beta (T_{bol} - T_{bas}) &= 0\,, \end{aligned} \tag{7}$$

and

$$
\begin{aligned}
\operatorname{div}(\kappa \operatorname{grad} T_{inc}) - c_b(\, W[T_{inc}+T_{bas}]T_{inc} & \\
+(\, W[T_{inc}+T_{bas}] - W[T_{bas}]\,)\,(T_{bas}-T_b)\,) + Q_e &= 0\,, \\
\kappa \frac{\partial T_{inc}}{\partial n} + \beta T_{inc} &= 0\,.
\end{aligned}
\tag{8}
$$

This splitting allows us to distinguish clearly between local effects forced by the permanent cooling of the human body at the surface and the heating by the electromagnetic field. Therefore, in an adaptive approach most of the refinement can be concentrated in regions where the power Q_e is large.

For the temperature dependence of blood perfusion we slightly simplified the curves presented in [17]. For healthy tissue (muscle and fat) we assume sigmoidal curves consisting of a Gaussian profile describing the perfusion increase between $37°C$ and $45°C$, and a plateau for temperatures above $45°C$ (see Fig. 1). In the raising part our curve differs only slightly from the one used in [17], the differences are small compared to the uncertainties of the underlying experimental data [16]. In [17] a decrease of perfusion above 45°C is assumed. This is motivated by the observation that vasculature is destroyed if tissue is heated to such temperatures for about 30 minutes. We do not assume such a decrease of perfusion. Normally, this should not matter because our object function for optimization (see Sect. 2.2) guarantees that temperatures in healthy tissue are always below 45°C. The curve we assume for fat tissue takes into account that fat tissue has a smaller capability to increase perfusion than muscle tissue. For tumor tissue we use a curve with the same shape as the curve for tumor core used in [17]. We choose slightly different absolute values to make the results comparable with prior studies assuming constant–rate perfusion. Our absolute values for blood perfusion are open for discussion, and the capability to increase perfusion also strongly depends on the cardiac state of the individual patient. But in this study we are mainly interested in qualitative effects of temperature–dependent blood flow.

The material properties of the involved tissues are summarized in Tab. 1. For blood we take $T_b = 37^o C$ and $c_b = 3500 Ws/kg/^o C$. If a constant–rate perfusion model is applied, we assume mean perfusion values for muscle, $W_{muscle} = 2.3 kg/s/m^3$, and fat, $W_{fat} = 0.54 kg/s/m^3$. The maximal value $W_{tumor} = 0.833 kg/s/m^3$ is taken for tumor tissue.

Temperature–dependent blood perfusion in muscle:

$$W_{muscle} = \begin{cases} 0.45 + 3.55 \exp\left(-\dfrac{(T-45.0)^2}{12.0}\right), & T \leq 45.0 \\ 4.00\,, & T > 45.0 \end{cases} \tag{9}$$

Temperature–dependent blood perfusion in fat:

$$W_{fat} = \begin{cases} 0.36 + 0.36 \exp\left(-\dfrac{(T-45.0)^2}{12.0}\right), & T \leq 45.0 \\ 0.72\,, & T > 45.0 \end{cases} \tag{10}$$

Temperature–dependent blood perfusion in tumor:

$$W_{tumor} = \begin{cases} 0.833\,, & T < 37.0 \\ 0.833 - (T-37.0)^{4.8}/5.438E{+}3\,, & 37.0 \leq T \leq 42.0 \\ 0.416\,, & T > 42.0 \end{cases} \tag{11}$$

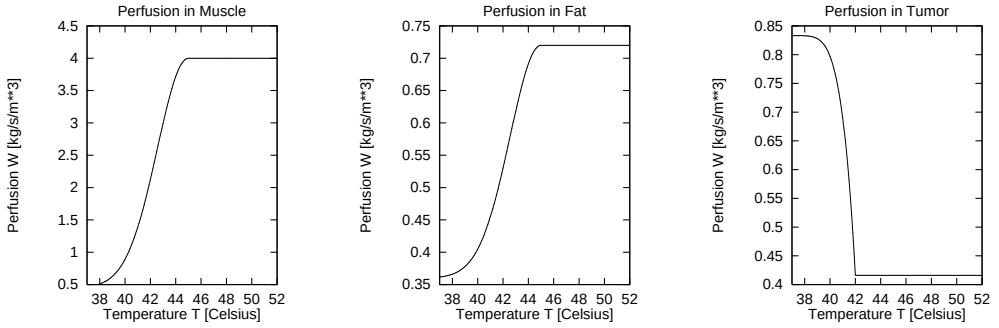

Fig. 1: Nonlinear models of temperature–dependent blood perfusion for muscle tissue, fat tissue, and tumor.

Tissue	Thermal conductivity κ $[W/m/^\circ C]$	Electric conductivity σ $[1/m/\Omega]$	Density ρ $[kg/m^3]$	Specific heat c $[Ws/kg/^\circ C]$	Mass flow rate W $[kg/s/m^3]$
Fat	0.210	0.04	900	3,500	W_{fat} (10)
Tumor	0.642	0.80	1,000	3,500	W_{tumor} (11)
Bladder	0.600	0.60	1,000	3,500	5.000
Kidney	0.577	1.00	1,000	3,500	66.670
Liver	0.640	0.60	1,000	3,500	16.670
Muscle	0.642	0.80	1,000	3,500	W_{muscle} (9)
Bone	0.436	0.02	1,600	1,000	0.540
Aorta	0.506	0.86	1,000	3,500	83.330
Intestine	0.550	0.60	1.000	3,500	3.333

Tab. 1: Material properties of tissues.

2.2 Object Function for Optimization

Our goal is to control the amplitudes z_j, $j = 1, \ldots, N_{chan}$, of the independent channels in order to achieve an effective hyperthermia therapy. A favourable temperature distribution is characterized as follows:

- Within the tumor a therapeutic temperature level of $42 - 43^oC$ is reached.
- No larger regions of healthy tissue are heated to above $42 - 43^oC$.
- Temperature in healthy tissue does not exceed certain temperature limits depending on the tissue type.

Taking into account these requirements we define an object function for optimization

$$q = \int\limits_{\substack{x \in \text{ tumor} \\ T < T_{ther}}} (T_{ther} - T)^2 \, dx \; + \int\limits_{\substack{x \notin \text{ tumor} \\ T > T_{health}}} (T - T_{health})^2 \, dx \; + \; p \int\limits_{\substack{x \notin \text{ tumor} \\ T > T_{lim}}} (T - T_{lim})^2 \, dx \; , \quad (12)$$

where we use a therapeutic level $T_{ther} = 43^oC$, and a temperature $T_{health} = 42^oC$ that should not be exceeded in healthy tissue. The limits T_{lim} are chosen tissue–dependent: $T_{lim} = 42^oC$ for more sensible tissue compartments (bladder, intestine) and $T_{lim} = 44^oC$ otherwise. To ensure high penalization for temperatures exceeding the limits we set $p = 1000$.
The definition of the object function as an integral of squares guarantees that

regions with large deviations from the desired temperatures, i.e., "hot spots" in healthy tissue and "cold spots" in the tumor, contribute large amounts to the object function. A similar optimization strategy for a phased array hyperthermia system based on a simpler object function is described in [13]. In contrast to the object function proposed there, we add the second term which effectively avoids excessive heating of healthy tissue. Moreover, we evaluate the object function not only in a small number of selected points, but for the entire three–dimensional temperature distribution.
Optimization of the temperature distribution means to choose the amplitudes z_j for each channel in such a way that the resulting temperature field minimizes the object function q.

3 Adaptive Numerical Algorithm

3.1 Grid Generation

For the numerical solution of the nonlinear heat transfer equation we use the *finite element method*. As a prerequisite we need a three–dimensional geometric model in which the different tissue compartments are represented. In this section we describe briefly how to generate such a model based on a set of CT-scans of a patient. Prior to grid generation, a segmentation of the CT data is performed, i.e., the relevant tissue compartments are defined on each scan.
Our method for generating a patient model consists of three steps:
First we extract the compartment surfaces from the segmented CT data. For this purpose we have generalized the well–known marching cubes algorithm [12] for non-binary classifications [9]. Our method creates a consistent description of the compartment interfaces. They are composed of so-called patches each separating two different compartments.
Second we simplify the surfaces to make them suitable for tetrahedra generation. We have extended an algorithm from computer graphics [6] to avoid intersections and assure a high quality (i.e. aspect ratio) of the surface triangles.
Third we fill each tissue compartment with tetrahedra using an advancing front algorithm. The compartment's surface is composed from the corresponding patches. At the beginning we start with this surface. Then repeatedly a triangle of the advancing front is selected and a fourth point is searched such that the resulting tetrahedron resembles an equilateral one as much as possible. This procedure is continued until the whole compartment is filled with tetrahedra [15].

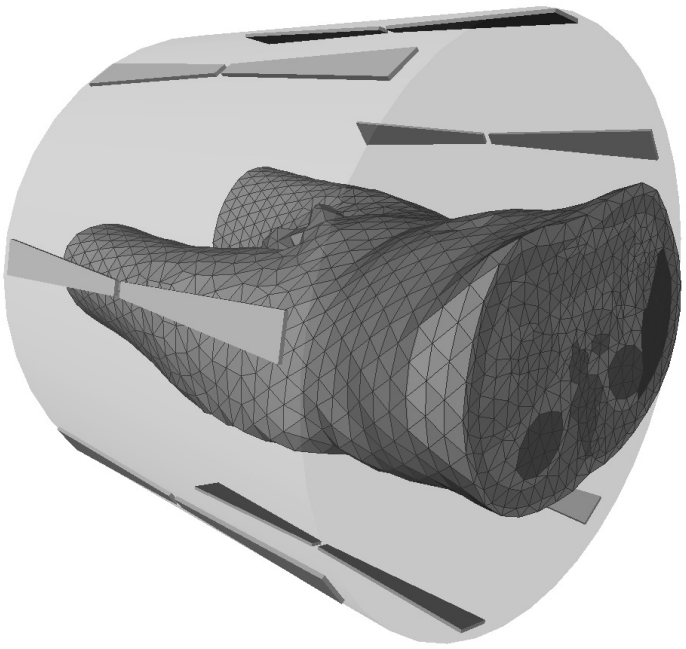

Fig. 2: Patient model (torso) and hyperthermia applicator. The patient is surrounded by 8 antennas emitting radiowaves. A water–filled bolus is placed between patient and antennas.

3.2 Time and Space Discretization

The principle difficulties in numerically solving the bio–heat transfer equation (1) are the nonlinearity due to the perfusion term and the different material properties of the tissues. Using a linearly implicit method of Rosenbrock type for the time discretization [8] and adaptive finite elements in space, we are able to integrate the heat equation efficiently. Within this approach, the approximate temperature T_n at time t_n is constructed by a linear combination of the previous temperature T_{n-1} at time t_{n-1} and different intermediate values $\triangle T_n^j, j = 1, 2, 3$, namely

$$T_n = T_{n-1} + \sum_{j=1}^{3} b_j \triangle T_n^j \ . \tag{13}$$

These values $\triangle T_n^j$ are determined by the following linear elliptic boundary value

problems:

$$\frac{\rho c}{\gamma \triangle t_n} \triangle T_n^j - \operatorname{div}(\kappa \operatorname{grad} \triangle T_n^j) + c_b\, JF[T_{n-1}]\, \triangle T_n^j \;=$$

$$\operatorname{div}(\kappa \operatorname{grad} T_n^j) - c_b\, F[T_n^j] + \frac{\rho c}{\triangle t_n} \sum_{i=1}^{j-1} c_{ji}\, \triangle T_n^i + Q \quad \text{in } \Omega\,, \tag{14}$$

$$\kappa \frac{\partial}{\partial n} \triangle T_n^j = \beta\,(T_{out} - \triangle T_n^j) \quad \text{on } \partial\Omega\,, \tag{15}$$

with

$$T_n^j := T_{n-1} + \sum_{i=1}^{j-1} a_{ji}\, \triangle T_n^i\,,\; JF := \frac{\partial F}{\partial T}\,,\; \triangle t_n := t_n - t_{n-1}\,.$$

The solution process for the intermediate temperatures $\triangle T_n^j$ can be done successively because the sums in the right–hand side of (14) extend to $j-1$ only. The coefficients γ, a_{ji}, c_{ji}, and b_j are chosen such that the method reaches order three in time and has good stability properties [8].
To compute the basal temperature T_{bas} we set in (14)

$$F[T] = F_{bas}[T] := W[T](T - T_b), Q = 0, T_{out} = T_{bol}\,.$$

The problem for the temperature increment T_{inc} forced by the electric field is solved with

$$F[T] = F_{inc}[T] := (W[T + T_{bas}] - W[T_{bas}])(T_{bas} - T_b) + W[T + T_{bas}]T$$

$$Q = Q_e, T_{out} = 0\,.$$

The linear elliptic problems (14) have to be solved for each intermediate value $\triangle T_n^j$. We apply a continuous finite element discretization in space to ensure the continuity of the temperature and its fluxes at the inner tissue boundaries.
The starting point of the finite element method is the weak formulation of (14). We seek for piecewise linear solutions. Let S_h^1 consist of all continuous functions which are polynomials of first order on each finite element, then the finite element solutions $\triangle_h T_n^j \in S_h^1$ have to satisfy the equations

$$(A_n \triangle_h T_n^j\,,\, \phi) = (r_n^j\,,\, \phi) \quad \forall \phi \in S_h^1,\; j = 1, 2, 3. \tag{16}$$

Here, $(\cdot, \cdot)$ represents the usual inner product, A_n is the weak representation of the differential operator on the left–hand side in (14) and includes the boundary conditions. The function $r_n^j = r_n^j(\triangle T_n^1, ..., \triangle T_n^{j-1})$ stands for the whole right–hand side of the j-th equation in (14). The operator A_n is independent of j, so that the method requires its calculation only once within each time step.

3.3 A Posteriori Error Estimates

The special structure of the employed Rosenbrock method (13) allows us to define a solution of second order using a simple embedding strategy:

$$\hat{T}_n = T_{n-1} + \sum_{j=1}^{3} \hat{b}_j \triangle T_n^j \tag{17}$$

with a different set of coefficients in (13). The difference between the two solutions $\|T_n - \hat{T}_n\| =: \varepsilon_n$ satisfactorily estimates the local error of the time discretization, and can be utilized to propose a new time step

$$\triangle t_{n+1} = \frac{\triangle t_n}{\triangle t_{n-1}} \left(\frac{TOL_t \, \varepsilon_{n-1}}{\varepsilon_n \, \varepsilon_n} \right)^{1/3} \triangle t_n \; . \tag{18}$$

This step size selection guarantees that the stationary solution is reached in a few steps with respect to a desired accuracy TOL_t [7].
To get a posteriori error estimates for the spatial discretization, we solve local Dirichlet problems on small subdomains. Let Q_ω be the set of all quadratic polynomials over ω which is the union of all tetrahedra having one common edge. Because we solve our elliptic problems (14) using linear elements, the local approximations e_n^j of the spatial errors

$$E_n^j := \triangle T_n^j - \triangle_h T_n^j \tag{19}$$

should be computed with at least the basis functions of Q_ω. Imposing homogenous Dirichlet boundary conditions, the approximate local errors related to all ω are represented by one degree of freedom at the midpoint of the corresponding edge [11]. Equipped with local errors of the intermediate values $\triangle T_n^j$, we can form error norms by

$$\|e_n\| = \|P\, T_{n-1} + \sum_{j=1}^{3} b_j \, e_n^j\| \, . \tag{20}$$

$P\, T_{n-1}$ is the projection error resulting from the fact that within an adaptive approach the grids for T_{n-1} and T_n in general are different.
We can get both local and global error informations taking Ω or ω to compute the norms in (20), for use in our adaptive mesh control algorithm. Local a posteriori error estimates are employed to decide which elements to refine or to unrefine. The aim of our mesh adaptation is to equilibrate the error until a final mesh is created in which all elements have approximately the same error, and a global prescribed accuracy TOL_x is reached.

3.4 Mesh Adaptation

For local mesh refinements we use regular partitions of tetrahedra as described in [3]. Here we summarize some fundamental facts.
By connecting the midpoints of the edges of a given tetrahedron t, we obtain four new tetrahedra each of which corresponds to a vertex of t. The remaining octahedron is split into four more tetrahedra (Fig. 3). This partition depends on the selection of the interior diagonal of the octahedron which can be chosen in three different ways. Each choice provides a regular refinement of the given tetrahedron.

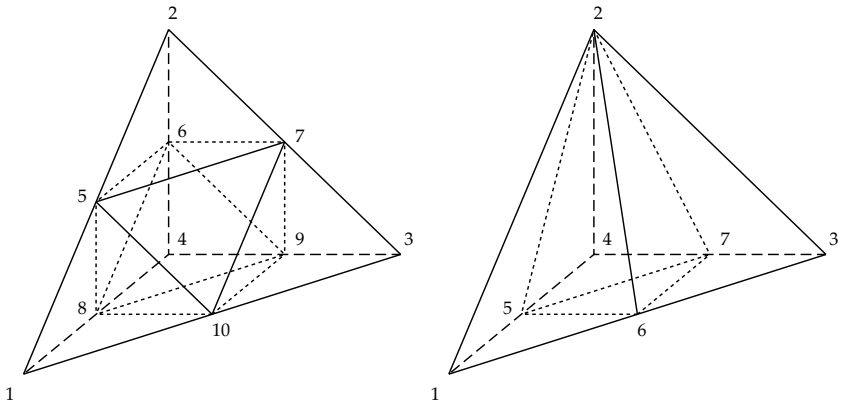

Fig. 3: Regular refinement of a tetrahedron (left) and one special closure (right).

By special choice of the interior diagonal [3] we ensure that the successive partitions of a tetrahedron are stable in the following sense: For each tetrahedron t the ratio of the diameter and the radius of the largest interior ball remains uniformly bounded during all refinement steps. After regular refinement we use special closures to avoid non-conforming vertices (see Fig. 3 for an example). To preserve the stability of the refinement process the resulting irregular tetrahedra are skipped at the beginning of further refinement. After an accepted time step the triangulation is coarsened [11].

3.5 Optimization

Using our piecewise linear finite element solution T_h which represents an approximation of the stationary temperature distribution on an adaptive spatial mesh M_h, and applying an integration formula based only on the vertices x_i (mass lumping), we get an approximation of the object function (12)

$$q_h = \sum_{i \in M_{h1}} \frac{w_i}{4}(T_{ther} - T_h(x_i))^2 + \sum_{i \in M_{h2}} \frac{w_i}{4}(T_h(x_i) - T_{health})^2 + p \sum_{i \in M_{h3}} \frac{w_i}{4}(T_h(x_i) - T_{lim})^2 \tag{21}$$

with

$$\begin{aligned} M_{h1} &= \{i\colon\ x_i \in \text{tumor},\ T_h(x_i) < T_{ther}\}, \\ M_{h2} &= \{i\colon\ x_i \notin \text{tumor},\ T_h(x_i) > T_{health}\}, \\ M_{h3} &= \{i\colon\ x_i \notin \text{tumor},\ T_h(x_i) > T_{lim}\}, \end{aligned}$$

where w_i stands for the volume of all tetrahedra of which x_i is a vertex.
In a next step we derive formulas which allow us to compute quickly the temperature field for arbitrary amplitudes z_j. Let us first consider the linear model with a constant–rate perfusion in each tissue. Then from (8) it can be directly seen that T_{inc} depends linearly on the distribution of the absorbed power Q_e. Hence, a superposition principle is valid:

$$T_{inc}(\alpha_1 Q_e^{(1)} + \alpha_2 Q_e^{(2)}) = \alpha_1 T_{inc}(Q_e^{(1)}) + \alpha_2 T_{inc}(Q_e^{(2)})\,. \tag{22}$$

According to the representation (5) we get

$$T_{inc}(Q_e) = \sum_{j,k=1}^{N_{chan}} z_j^*\, T_{inc}(E_j^* E_k)\, z_k\ , \tag{23}$$

and finally for the whole stationary temperature distribution

$$T(Z) = T_{bas} + \sum_{j,k=1}^{N_{chan}} z_j^*\, T_{inc}(E_j^* E_k)\, z_k\ , \tag{24}$$

where Z is the vector of all z_j. The temperature increments $T_{inc}(E_j^* E_k)$ can be derived from N_{chan}^2 basic calculations combining two channels. Consequently, for an arbitrary set of parameters z_j the object function can be computed very fast. The same holds for the first and second derivatives of the finite element solution T_h with respect to the parameters z_j.
In the nonlinear case, relation (22) is no longer valid. Nevertheless, we can fix the nonlinear perfusion terms with respect to a given intermediate state Z_n of all amplitudes. Then we utilize representation (23) as an approximation in a neighborhood of Z_n to perform the minimization process. Doing so we get a better Z_{n+1} for which we solve the nonlinear heat equation. The arising perfusion $W(T(Z_{n+1}))$ is once again fixed and the optimization is done. Improving successively the constant–rate model of the perfusion in such a way, we end up with a

nearly optimal adjustment of the parameters z_j for the nonlinear model.
To start the optimization we calculate an initial optimized $Z_0^{(0)}$ employing our constant–rate perfusion model. Next we adjust the total power, i.e., we scale the amplitudes of $Z_0^{(0)}$ such that for the nonlinear model the maximal temperature in healthy tissue does not exceed 44^oC.
Employing a damped Newton method for the optimization, the iteration can be described as follows:

Choose initial value $Z_0^{(0)}$

for $n = 0, 1, \ldots$

Calculate stationary temperature $T(Z_n^{(0)})$

Calculate $W_n := W(T(Z_n^{(0)}))$

Calculate $T_{\text{inc}}(E_j^* E_k)$, $j, k = 1, \ldots, N_{\text{chan}}$, employing W_n

for $k = 0, 1, \ldots$

Calculate $D^i q_h := \left. \dfrac{D^i q_h}{dZ^i} \right|_{Z = Z_n^{(k)}}$, $i = 1, 2$

Calculate $\Delta Z := -(D^2 q_h)^{-1} D^1 q_h$

Find $\alpha_0 \in \{1, \frac{1}{2}, \frac{1}{4}, \ldots\}$ **such that**

$q_h(Z_n^{(k)} + \alpha_0 \Delta Z) < q_h(Z_n^{(k)}) + \frac{1}{2} \alpha_0 D^1 q_h \Delta Z$

Define $Z_n^{(k+1)} := Z_n^{(k)} + \alpha_0 \Delta Z$

Finished?

Define $Z_{n+1}^{(0)} := Z_n^{(k+1)}$

Finished?

The inner iteration is terminated if the object function has changed by less than 0.02 within the last 10 iterations. To control the outer iteration we always compute the new stationary temperature $T(Z_{n+1}^{(0)})$ and compare it with the old one. If the difference becomes small enough (less than 0.05^oC), we stop the optimization process.

4 Numerical Results

4.1 Optimization

We report some data concerning optimization processes for two individual patients. The simulations were done for the Sigma 60 Applicator of the BSD 2000 Hyperthermia System which consists of eight radio frequency antennas grouped in four antenna pairs. Each group can have its own amplitude and phase. So, our aim is to control four different complex values z_j.
The patients have different tumor locations. Fig. 4 shows specific sagittal and transversal sections of both patients where the contours of bone and tumor are colored black and grey, respectively. It can be clearly seen that the tumor of the second patient is strongly shielded by bones whereas the first tumor is located in a more central position.
For both patients the optimization comes to an end after five outer iteration steps. The corresponding values of the object function q_h and the maximal temperature difference are shown in Tab. 2. We state that the values of the object function are reduced by nearly the same factor 2/3.

	n	0	1	2	3	4	5
Patient 1	q_h	1,732	1,458	1,327	1,263	1,229	1,214
	$\|\delta T\|_\infty$	-	3.5	0.7	0.18	0.085	0.043
Patient 2	q_h	4,264	2,743	2,796	2,813	2,819	2,823
	$\|\delta T\|_\infty$	-	3.2	0.3	0.15	0.077	0.044

Tab. 2: History of object function q_h and maximal temperature difference during the optimization process.

In Fig. 5 the convergence history of the vector $Z_n^{(0)}$ and the object function q_h is presented. For each outer iteration step all complex amplitudes z_j are plotted as vertices of a quadrilateral. We observe that the use of the nonlinear heat transfer model leads to a more uniform adjustment of $|z_j|$ and to a slight reduction of the phase differences. Moreover, the phases of the antenna pairs at the left and right of the patient come successively closer. They can be identified in the diagrams as neighbors of the channel with fixed phase zero. So, we get a more symmetric adjustment of the phases.

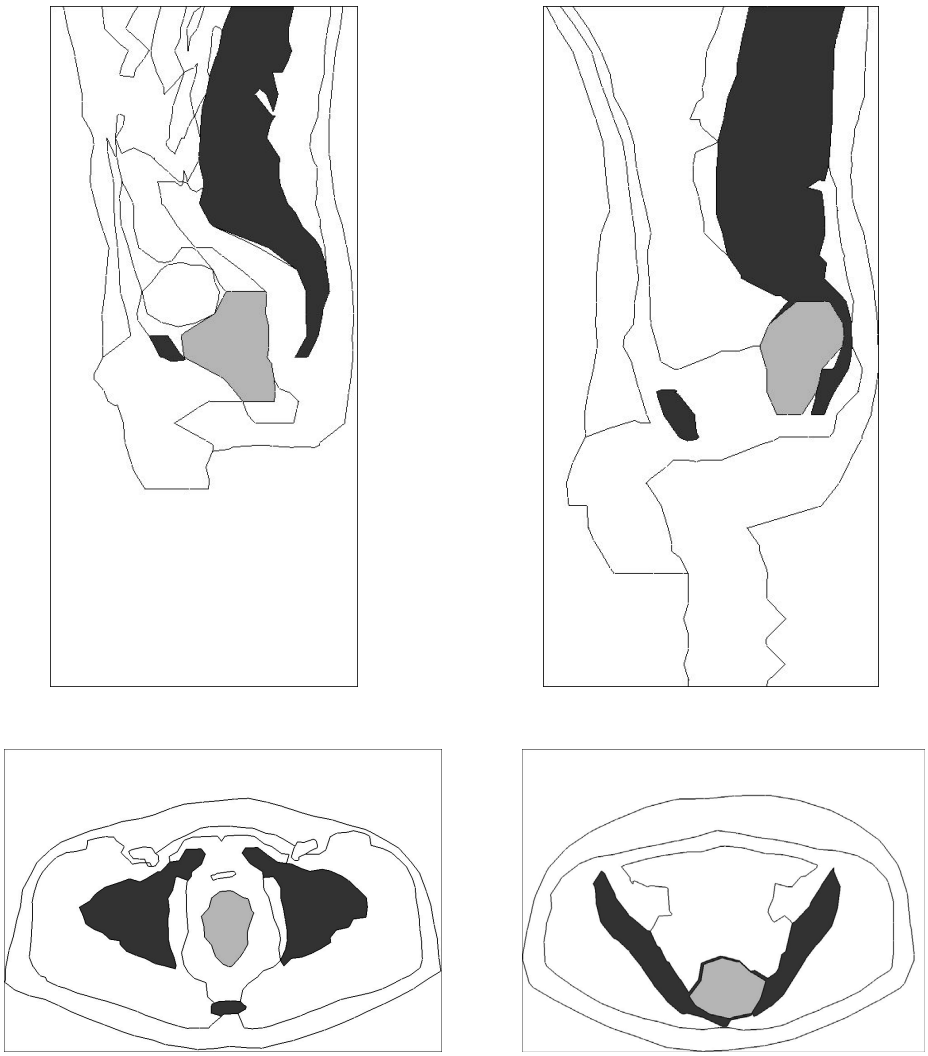

Fig. 4: Contours of tissue compartments in specific sagittal (top) and transversal (bottom) sections. The location of tumors (grey) with respect to bone (black) is shown for the first patient (left) and the second patient (right).

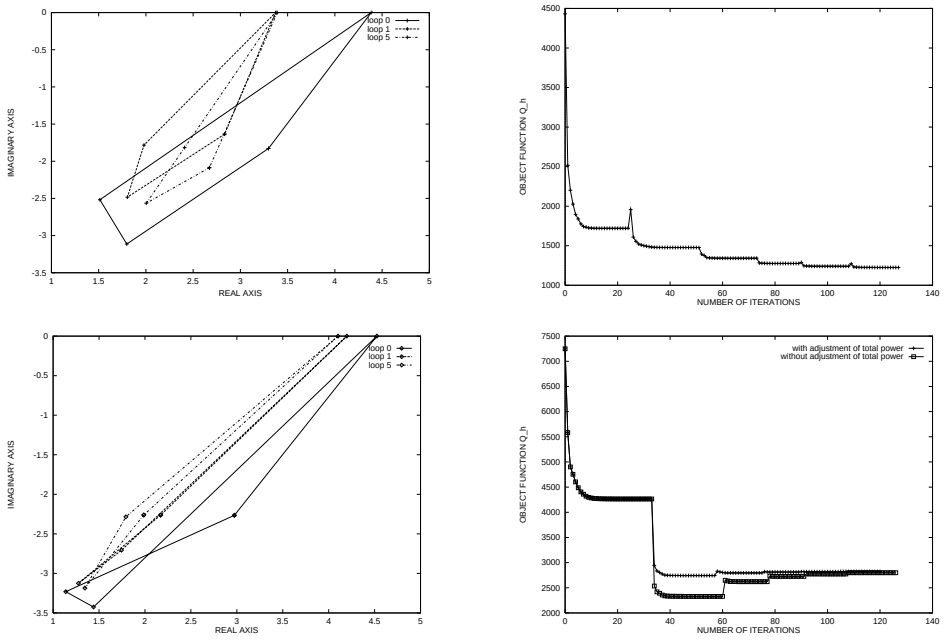

Fig. 5: Patient 1 (top) and patient 2 (bottom). Optimization of the four complex amplitudes plotted in a quadrilateral for each outer iteration step (left); minimization history of the object function q_h (right).

The optimization process starts with a synchronous steering of all antennas resulting in $q_h = 4,430$ for the first patient and $q_h = 7,250$ for the second. Each loop starts with an update of the constant–rate perfusion model causing a jump in the values of the object function. To test the robustness of our optimization process we slightly changed the strategy for the second patient in an additional computation. After the initial loop we did not adjust the total power as described in Section 3.5. This resulted in a better value of q_h at the beginning, but ended at the same final solution (see Fig. 5).

The smaller values of the object function for the nonlinear model (see Tab. 2) result from a better tumor heating, which is reflected by the temperature–volume histograms for tumor tissue shown in Fig. 6. The histograms for muscle tissue reveal that assuming the nonlinear model a much larger amount of tissue is heated to temperatures above 40^oC. The critical temperature region of muscle ($T > 42^oC$) is comparable for both patients. But the tumor heating of the first patient is much better. This is also reflected by the smaller value of the corresponding object function.

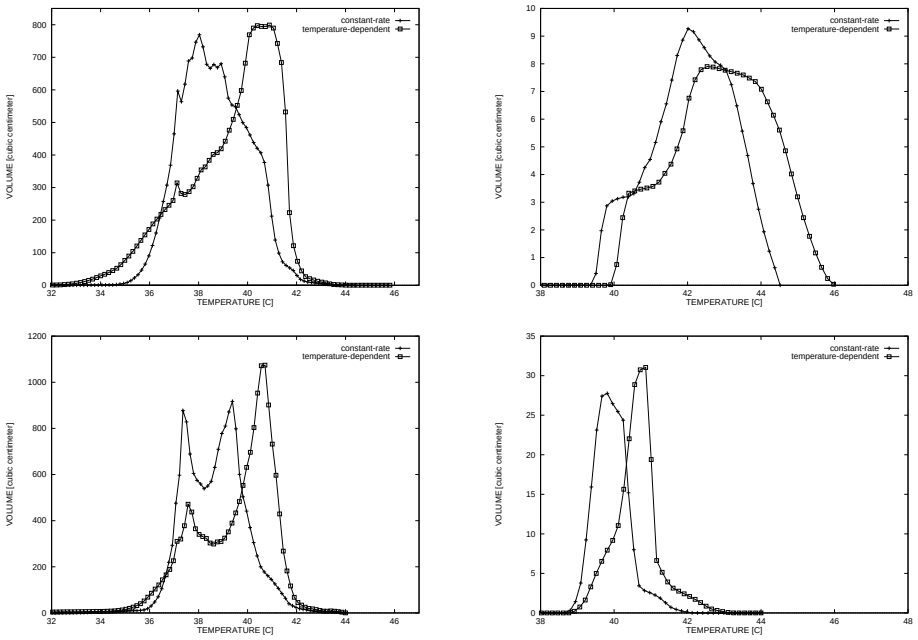

Fig. 6: Patient 1 (top) and patient 2 (bottom). Temperature–volume histograms for muscle (left) and tumor tissue (right) showing the differences between constant–rate and temperature–dependent perfusion.

4.2 Effects of Mesh Adaptation

The optimized temperature distribution based on an adaptively improved spatial grid is compared with the temperature field computed on the coarse grid.
Fig. 7 shows two cuts through the computational domain of the second patient involving the tumor boundary to give an impression of the local refinement process. The coarse grid contains $7,140$ vertices (degrees of freedom for the finite element solution), while the refined grid has $35,936$ vertices. Starting with the coarse grid two refinement steps are necessary to reach an accuracy of 2%. The corresponding uniform grid would have about $420,000$ degrees of freedom which demonstrates the power of the proposed adaptive method.
Fig. 8 illustrates the influence of the adaptive mesh control on the adjustment of the antenna pairs and the object function. The optimization process based on the coarse grid requests five outer iteration loops and reaches a maximal temperature difference $\|\delta T\|_\infty = 0.03^o C$ at $q_h = 2,505$. Comparing the final value of the object function with that given in Tab. 2 for the fine mesh, $q_h = 2,823$, the attained change

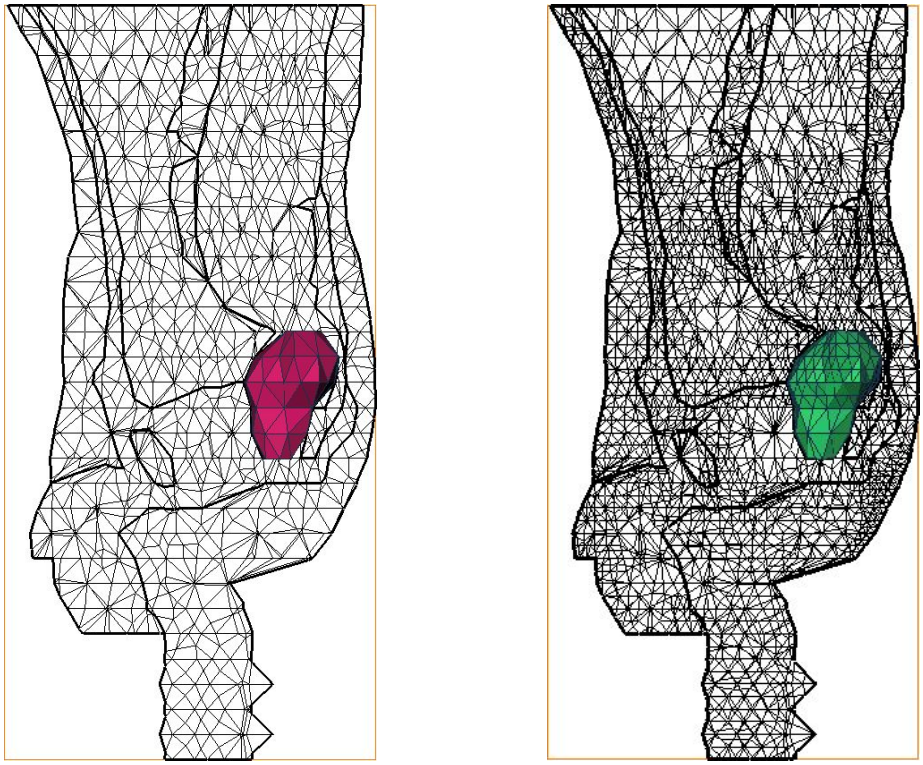

Fig. 7: Patient 2. Coarse (left) and refined (right) grid with tumor boundary used for the computation of the optimized temperature distribution.

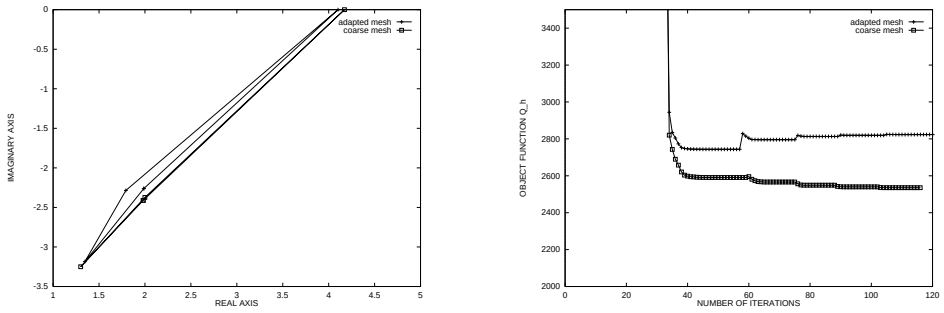

Fig. 8: Patient 2. Influence of the adapted mesh control on the optimized adjustment of the antenna pairs and the minimization history of the object function.

ranges in the order of 10%. This is also reflected by the adjustment of the applicator. The same difference can be observed for the temperature increment T_{inc} with respect to coarse and fine meshes. The local refinement controlled by a posteriori error estimates leads to a better resolution of the solution in regions with high temperature gradients and material transitions.

5 Conclusion

There are significant qualitative differences between the temperature distributions predicted by the linear and the nonlinear heat transfer model. Generally the self–regulation of healthy tissue reflected by the nonlinear model reduces "hot spots" caused by local maxima of the absorbed electromagnetic fields. This is one reason for the slightly better tumor heating (ca. 0.5°C) predicted by the nonlinear model (see the temperature–volume histograms for tumor tissue, Fig. 6). An analogous result is reported in [17] for ferromagnetic thermoseed hyperthermia. An important finding is that the nonlinear model has an impact on the optimal treatment parameters as well (see Fig. 5). The maximal changes of optimal parameters are 22° for the phases and 0.22 for the relative amplitudes.
In the future we will compare the simulations with clinical data to check if the nonlinear model is a more realistic representation of the heat transfer processes during regional hyperthermia. There are some effects which should be observable in the clinical data:

- The nonlinear model predicts that a significantly lower *total power* (ca. 340 W compared to ca. 430 W) is needed to achieve the optimal temperature distribution. In the simulations the total power is always limited by the requirement that the temperature in healthy tissue should not exceed 44°C.

- In superficial layers which are cooled by the water bolus the tissue temperature is lower than blood temperature. There blood acts as a heat source, not as a heat sink. For such regions the linear model assumes a much higher perfusion than the nonlinear one. Thus the *skin temperatures* predicted by the nonlinear model are ca. 2°C lower. An uncertainty for the comparison of simulated skin temperatures with clinical data is the heat transfer coefficient between body and water bolus. In our calculations we assumed 45 W/m^2/°C.

- The nonlinear model predicts that a much larger amount of muscle tissue is heated to above 40°C (see the temperature–volume histograms for muscle

tissue, Fig. 6). In spite of the fact that only a small number of temperature measurements from inside the body is available, this effect might be visible in clinical data.

The comparison of the results with real–life applications will lead to an assessment of the parameters used in our nonlinear model.
Finally, we note that first computations with an applicator consisting of 24 antennas have been performed. There is some hope to improve the temperature distribution especially for tumors that are strongly shielded by bones.

Acknowledgement. The authors are indebted to P. Deuflhard for his continuing support of this project and to R. Beck for providing the electric field data. We thank J. Gellermann and P. Wust from Klinikum Rudolf Virchow for fruitful discussions about clinical aspects.

References

[1] R. Beck, P. Deuflhard, H.-C. Hege, M. Seebass, D. Stalling, Numerical Algorithms and Visualization in Medical Treatment Planning, in H.-C. Hege and K. Polthier (eds.), *Visualization and Mathematics*, Springer-Verlag, Heidelberg, 1997, 303-328

[2] R. Beck, P. Deuflhard, R. Hiptmair, B. Wolmuth, R.H.W. Hoppe, Adaptive Multilevel Methods for Edge Element Discretizations of Maxwell's Equations, Preprint SC 97–66, Konrad–Zuse–Zentrum für Informationstechnik Berlin, Germany, 1997

[3] F. Bornemann, B. Erdmann, R. Kornhuber, Adaptive multilevel methods in three space dimensions, *Int. J. Num. Meth. Engrg.* **36**, 3187–3203, 1993

[4] B. Erdmann, J. Lang, R. Roitzsch, *KASKADE – Manual*, Technical Report TR 93–05, Konrad–Zuse–Zentrum für Informationstechnik Berlin, Germany, 1993

[5] B. Erdmann, J. Lang, M. Seebass, Adaptive Solutions of Nonlinear Parabolic Equations with Application to Hyperthermia Treatments, in *Proc. Int. Symp. on Advances in Comp. Heat Transfer*, Cesme, 1997

[6] M. Garland, P.S. Heckbert, Surface Simplification Using Quadric Error Metrics, in *Computer Graphics Proceeding*, Addison Wesley, 1997, 209-216

[7] K. Gustafsson, Control of Error and Convergence in ODE Solvers, Ph.D. Thesis, Department of Automatic Control, Lund Institute of Technology, 1992

[8] E. Hairer, G. Wanner, *Solving Ordinary Differential Equations II, Stiff and Differential–Algebraic Problems*, Springer, Berlin–Heidelberg, 1991

[9] H.-C. Hege, M. Seebass, D. Stalling, M. Zöckler, A Generalized Marching Cubes Algorithm Based On Non-Binary Classifications, Preprint SC 97–05, Konrad–Zuse–Zentrum für Informationstechnik Berlin, Germany, 1997

[10] A. Kotte, J. van Leeuwen, J. de Bree, J. van der Koijk, H. Crezee, J. Lagendijk, A description of discrete vessel segments in thermal modelling of tissues, *Phys. Med. Biol.* **41**, 865–884, 1996

[11] J. Lang, Adaptive FEM for Reaction–Diffusion Equations, *Appl. Numer. Math.* 26, 105–116, 1998

[12] W.E. Lorensen, H.E. Cline, Marching Cubes: A high resolution 3D surface construction algorithm, *Computer Graphics* **21**, 163-169, 1987

[13] K.S. Nikita, N.G. Maratos, N.K. Uzunoglu, Optimal Steady–State Temperature Distribution for a Phased Array Hyperthermia System, *IEEE Trans. Biomed. Engrg.* **40**, 1299–1306, 1993

[14] H.H. Pennes, Analysis of tissue and arterial blood temperatures in the resting human forearm, *J. Appl. Phys.* **1**, 93–122, 1948

[15] M. Seebass, D. Stalling, J. Nadobny, P. Wust, R. Felix, P. Deuflhard, Three-Dimensional Finite Element Mesh Generation for Numerical Simulations of Hyperthermia Treatments, in C. Franconi, G. Arcangeli, and R. Cavaliere (eds.), *Proc. 7th Int. Congress on Hyperthermic Oncology, Roma* Vol. 2, 547-548, 1996

[16] C.W. Song, A. Lokshina, J.G. Rhee, M. Patten, S.H. Levitt, Implication of Blood Flow in Hyperthermic Treatment of Tumors, *IEEE Trans. Biomed. Engrg.* **31**, 9–16, 1984

[17] D.T. Tompkins, R. Vanderby, S.A. Klein, W.A. Beckman, R.A. Steeves, D.M. Frey, B.R. Palival, Temperature–dependent versus constant–rate blood perfusion modelling in ferromagnetic thermoseed hyperthermia: results with a model of the human prostate, *Int. J. Hyperthermia, Vol.* **10**, No. 4, 517–536, 1994

[18] S. Weinbaum, L.M. Jiji, A new simplified bio–heat equation for the effect of blood flow on local average tissue temperature, *J. Biomech. Engrg. Trans. ASME* **107**, 131–139, 1985